processes

MDPI

Article

Utilizing Limestone Alone for Integrated CO_2 Capture and Reverse Water-Gas Reaction in a Fixed Bed Reactor: Employing Mass and Gas Signal Analysis

Iwei Wang, Shihui Wang and Zhenshan Li *

Key Laboratory for Thermal Science and Power Engineering of the Ministry of Education, Department of Energy and Power Engineering, Tsinghua University, Beijing 100084, China; iwwang@tsinghua.edu.cn (I.W.); wang-sh18@mails.tsinghua.edu.cn (S.W.)
* Correspondence: lizs@tsinghua.edu.cn

Abstract: The integrated CO_2 capture and utilization coupled with the reverse water-gas shift reaction (ICCU-RWGS) presents an alternative pathway for converting captured CO_2 into CO in situ. This study investigates the effectiveness of three calcium-based materials (natural limestone, sol-gel $CaCO_3$, and commercial $CaCO_3$) as dual-functional materials (DFMs) for the ICCU-RWGS process at intermediate temperatures (650–750 °C). Our approach involves a fixed-bed reactor coupled with mass spectrometry and in situ Fourier transform infrared (FTIR) measurements to examine cyclic CO_2 capture behavior, detailed physical and chemical properties, and morphology. The in situ FTIR results revealed the dominance of the RWGS route and exhibited self-catalytic activity across all calcium-based materials. Particularly, the natural limestone demonstrated a CO yield of 12.7 mmol g^{-1} with 100% CO selectivity and 81% CO_2 conversion. Over the 20th cycle, a decrease in CO_2 capture capacity was observed: sol-gel $CaCO_3$, natural limestone, and commercial $CaCO_3$ showed reductions of 44%, 61%, and 59%, respectively. This suggests inevitable deactivation during cyclic reactions in the ICCU-RWGS process, while the skeleton structure effectively prevents agglomeration in Ca-based materials, particularly in sol-gel $CaCO_3$. These insights, coupled with the cost-effectiveness of CaO-alone DFMs, offer promising avenues for efficient and economically viable ICCU-RWGS processes.

Keywords: integrated CO_2 capture and utilization; reverse water-gas shift reaction; self-catalytic ability; stability; selectivity

Citation: Wang, I.; Wang, S.; Li, Z. Utilizing Limestone Alone for Integrated CO_2 Capture and Reverse Water-Gas Reaction in a Fixed Bed Reactor: Employing Mass and Gas Signal Analysis. *Processes* **2024**, *12*, 1548. https://doi.org/10.3390/pr12081548

Academic Editor: Francesca Raganati

Received: 1 July 2024
Revised: 18 July 2024
Accepted: 22 July 2024
Published: 24 July 2024

1. Introduction

A series of environmental issues in terms of the excessive emission of CO_2 has sparked widespread concerns [1]. The control of greenhouse gas emissions through Carbon Capture, Utilization, and Storage (CCUS) is acknowledged as a pivotal method in mitigating CO_2 emissions, garnering significant attention within the global research community [2]. Nevertheless, the CCUS process typically includes the capture, pressurized liquefaction, transportation, and conversion of CO_2, rendering the entire CO_2 reduction procedure intricate and costly. To simultaneously alleviate CO_2 emissions and energy consumption, a novel concept known as integrated carbon capture and utilization (ICCU) has been proposed [3–5]. In contrast to conventional CCUS methods, which treat CO_2 capture from flue gas [6] and CO_2 hydrogenation into liquid fuels as separate processes [7,8], ICCU eliminates the need for compression, liquefaction, and transportation of CO_2. This integration reduces energy losses associated with multiple temperature fluctuations and has the potential to enhance overall energy efficiency [9]. Noteworthy ICCU technologies currently under extensive study encompass CO_2 capture coupled with in situ methanation [10,11], dry reforming of methane (DRM) [12,13], and the reverse water gas shift reaction (RWGS) [14,15]. In the ICCU-RWGS process, CO_2 and H_2 are introduced separately for CO_2 capture in the flue gas and hydrogenation via water electrolysis, as shown in Figure 1. With the

introduction of H_2 during the utilization phase, the captured CO_2 liberated from sorbents is directly reduced and converted in situ to yield CO in a single reactor. Additionally, research has demonstrated that the hydrogen-to-carbon ratio in ICCU-RWGS can surpass the thermodynamic constraints of traditional RWGS, yielding a more favorable ratio for utilization as a feedstock in the Fischer–Tropsch Synthesis (FTS) process [16,17]. Consequently, ICCU-RWGS emerges as a preferable option for reducing the expenses of the CO_2 compression and transportation mid-process while concurrently enhancing the environmental and economic advantages of producing high-value-added chemicals.

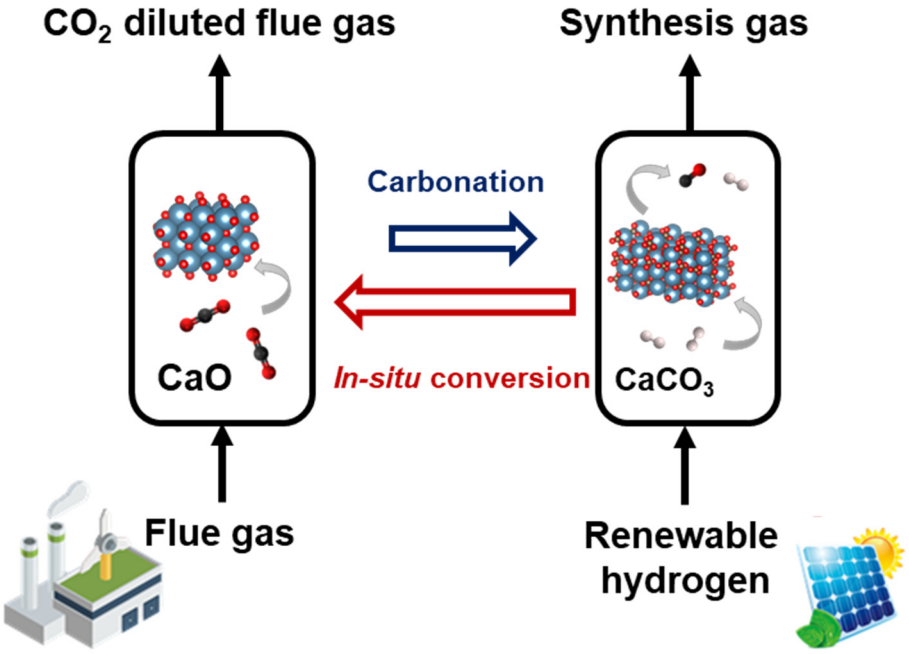

Figure 1. Schematic diagram of integrated CO_2 capture and utilization.

One major challenge of ICCU-RWGS technology revolves around the advancement of dual-function materials (DFMs) that encompass both CO_2 adsorbent and catalyst functionalities. Specifically, alkali and alkaline metal oxides or carbonates, such as CaO [18], SrO [19], MgO [20], Na_2CO_3, Na_2O, K_2O, and K_2CO_3 [21], operating within a temperature range from ambient to 900 °C have been utilized as CO_2 adsorbents within DFMs. The catalytic elements embedded in these DFMs predominantly include noble metals (Ru, Rh) [22,23] and transition metals (Ni, Fe, Co) [15,24]. To align with the reaction temperatures (600–800 °C) required for the RWGS process, high-temperature adsorbents like CaO, BaO, and SrO are commonly employed [19,25,26]. When evaluating DFMs, several essential criteria come into play, including high CO_2 sorption capacity, elevated CO_2 conversion rates, superior product selectivity, and robust operational stability. In particular, CaO stands out as a widely employed high-temperature CO_2 adsorbent, showcasing self-catalytic activities during the carbonate hydrogenation process [27,28]. This inherent functionality not only enhances the process's viability for commercialization but is also cost effective, abundant, and environmentally sustainable. Furthermore, utilizing CaO alone for high-purity syngas production has demonstrated noteworthy results, with a CO yield of 4.15 mmol/g-CaO, up to 75% CO_2 conversion, and 100% CO selectivity achievable at 700 °C within a fixed bed system [29]. Research on limestone hydrogenation under fluidized and isothermal conditions via a micro-fluidized bed thermogravimetric analysis coupled with mass spectrometry (MFB-TGA-MS) system has yielded promising outcomes, achieving 79.1% CO_2 conversion and approximately 100% CO selectivity at 710 °C [30]. These pioneering studies suggest the feasibility of utilizing the ICCU-RWGS process in conjunction with CaO-alone materials without necessitating additional catalytic components. However, despite the

success of $CaCO_3$/CaO material systems as DFMs within ICCU technology, further detailed exploration into their catalytic efficacy and stability is warranted.

From a reactor standpoint, traditional techniques such as thermogravimetric analysis (TGA) [31,32], packed-bed reactors [33–37], and MFB-TGA-MS [30,38] under fluidized conditions are the primary methods for analyzing integrated CO_2 capture and utilization-reverse water gas shift (ICCU-RWGS) processes. In fixed-bed reactors, high reactivity and stability are observed under isothermal conditions at 650 °C using a $Ca_1Ni_{0.1}Ce_{0.033}$ catalyst, which demonstrates a notable CO_2 capture capacity of 14.10 mmol CO_2 g^{-1} and a CO production rate of 7.3 mmol CO g^{-1} without deactivation over 20 cycles [39]. A nickel-cerium-based CaO material synthesized via the sol-gel method exhibits a CO_2 capture capacity of 15.34 mmol CO_2 g^{-1} and a CO production rate of 5.97 mmol CO g^{-1}, although it experiences an 11.6% loss in capacity over 10 cycles in a fixed-bed reactor [40]. Under fluidized and isothermal conditions, non-catalytic gas–solid reactions ($CaO + CO_2 \rightarrow CaCO_3$) coexist with catalytic gas–solid reactions ($CO_2 + H_2 \rightarrow CO + H_2O$), resulting in the gradual coating of Cu particles by $CaCO_3$ during carbonation. This phenomenon prevents Cu sintering but slightly reduces catalytic activity [41]. For material screening, fixed-bed reactors are primarily used in the ICCU field due to their ease of operation and convenience.

Therefore, understanding the reactive pathway, performance, and cyclic stability of calcium-based materials without additional catalyst components in ICCU-RWGS is urgent. To gain a deeper understanding of DFMs, particularly those derived from CaO-alone material, this study presents novel investigations through a comparative analysis conducted in a fixed-bed reactor coupled with mass spectrometry, employing mass and gas signal analysis. The study focuses on three calcium-based sorbents: natural limestone, commercially available carbonate, and synthetic materials (sol-gel $CaCO_3$). Furthermore, the research points out the reaction pathway through temperature-programmed surface reactions, employing in situ Fourier transform infrared (FTIR) spectroscopy to uncover the impact of ICCU temperature variations. The carbon capture and utilization process involving the three materials was evaluated across a temperature range spanning 650 to 750 °C, with increments of 25 °C. By examining these materials at different temperatures, the study aims to provide fresh insights into the strategic design of robust solid DFMs tailored for ICCU applications. Overall, the cost-effectiveness of CaO-alone DFMs offers promising pathways for efficient and economically viable ICCU-RWGS processes.

2. Experimental

2.1. Material Preparation

Natural limestone (Hubei Jingmen Shunzhan Cement Industrial Corp., Hubei, China), commercial $CaCO_3$ (98%, Shanghai Titan Scientific Corp., Shanghai, China), and sol-gel $CaCO_3$ were used for Ca-Based DFMs in the ICCU-RWGS process. Specifically, the sol-gel $CaCO_3$ was synthesized through a simple one-pot sol-gel method [41]. Calcium nitrate tetrahydrate ($Ca(NO_3)_2{\cdot}4H_2O$) with citric acid at a molar ratio of 1:2.5 (sum of metal cations/citric acid) was dissolved in 80 mL deionized water at room temperature. This was followed by mixing the dissolved cations with ethylene glycol at a molar ratio of 1.5:1 (ethylene glycol/citric acid) at 40 °C. The mixture was then heated at 80 °C to form a gel. The precursor gel was dried at 110 °C overnight and then calcined in a box furnace at 800 °C with airflow. The precursor particle was finally carbonated in the tube furnace with 15% CO_2 at 550 °C for 1 h to obtain the sol-gel $CaCO_3$. After crushing and grinding, the three nominated DFMs (natural limestone, commercial $CaCO_3$, and sol-gel $CaCO_3$) were carefully sieved to particle size ranges of 250–450 μm.

2.2. Material Characterization

X-ray diffraction (XRD) patterns (2 theta: 20°–70°) were obtained using a D8 Advance diffractometer with Cu Kα radiation with a continuous scanning rate of 2 degree min^{-1}. Scanning electron microscope (SEM) images and energy-dispersive spectroscopy (EDX) mappings were recorded on a scanning transmission electron microscope (Zeiss Merlin,

Oberkochen, Germany). Raman spectra was carried out using a Raman spectrometer (LabRAM HR Evolution, Horiba, Japan) with a He-Ne green laser (532 nm). The elemental compositions of natural limestone were quantified on inductively coupled plasma-optical emission spectroscopy (ICP-OES, ICAP 7400). The carbon and sulfur content of natural limestone was detected by the Carbon/Sulfur Analyzer (ELTRA CS-800).

2.3. Temperature Programmed Procedure

The H_2 temperature-programmed surface reaction (H_2-TPSR) was performed on the DFMs after the removal of surface species at 150 °C in a 30 mL min^{-1} N_2 (100 vol%) flow for 30 min. All of the DFMs were then heated from 150 °C to 850 °C in a H_2/N_2 (10 vol%) flow. The gaseous products were collected online using a Fourier transform infrared (FTIR) spectrometer (Thermo Nicolet iS20) equipped with a gas cell to track the gas signals, including CO, CO_2, CH_4, H_2O.

2.4. Integrated CO_2 Capture and Utilization System

The performance evaluation for CO_2 capture and in situ hydrogenation to CO was performed in a fixed-bed system coupled mass spectrometry. As shown in Figure 2a, the system consists of a quartz reactor, an electric furnace, a gas supply system, and a measuring system. The quartz reactor (od: 23 mm, id: 20 mm, L: 1000 mm) is designed to be a fixed bed, and a porous quartz plate with a thickness of 5 mm is used as the gas distributor. The reactor was heated by an external electric furnace with the temperature monitored by a K-type thermocouple. For the bed temperature, one K-type thermocouple was measured in the material layer. The gas flow rate was controlled with a mass flow control (MFC, Sevenstar, Beijing, China). The composition of the effluent stream was monitored by an online gas mass spectrometry (Tilon LC-D200M). The entire quartz reactor without contacting any part of furnace rests entirely on the weighing transducer (XPE 1203S, Mettler Toledo Corp., Zürich, Switzerland) to measure the real-time mass signals with a readability of 1 mg. Based on the gas profile and mass signals, the precise conversion information of ICCU would be effectively obtained. As shown in Figure 2b, to ensure the consistency of gas signal and mass signal on samples, the obtained data would be verified whether in the ±10% error margin. This indicates that the gas signals and mass signals as a function of time were also confirmed during CO_2 capture and in situ hydrogenation steps.

Typically, DFMs were heated to specified temperature with a rate of 30 °C/min in Ar (200 mL/min). After the temperature is stabilized, switch Ar to 15 vol% CO_2/Ar (200 mL/min) for 30 min CO_2 capture. The DFMs were then purged in Ar (200 mL/min) for 5 min, following with in situ hydrogenation in pure H_2 (200 mL/min) for 30 min.

Furthermore, the CO formation (q_{CO}), CH_4 formation (q_{CH_4}), and CO_2 formation (q_{CO_2}) were calculated from the gas profile via Equations (1)–(3).

$$q_{CO}[\text{mmol g}^{-1}] = \frac{1}{W}\int_{t_{H_2,in}}^{t_{H_2,out}} F_{CO,out}(t)dt \quad (1)$$

$$q_{CH_4}[\text{mmol g}^{-1}] = \frac{1}{W}\int_{t_{H_2,in}}^{t_{H_2,out}} F_{CH_4,out}(t)dt \quad (2)$$

$$q_{CO_2}[\text{mmol g}^{-1}] = \frac{1}{W}\int_{t_{H_2,in}}^{t_{H_2,out}} F_{CO_2,out}(t)dt \quad (3)$$

where the $F_{CO,out}$, $F_{CH_4,out}$, and $F_{CO_2,out}$ are the molar flow rates of CO, CH_4, and CO_2 (mmol min^{-1}) in the outlet gas, respectively. W (g) is the sample mass.

Finally, the CO selectivity (S_{CO}), the CO_2 conversion (X_{CO_2}), and CO yield (Y_{CO}) were determined via Equations (4) and (5).

$$S_{CO} = \frac{q_{CO}}{q_{CO} + q_{CH_4}} \times 100\% \quad (4)$$

$$X_{CO_2} = \frac{q_{CO} + q_{CH_4}}{q_{CO} + q_{CH_4} + q_{CO_2}} \times 100\% \quad (5)$$

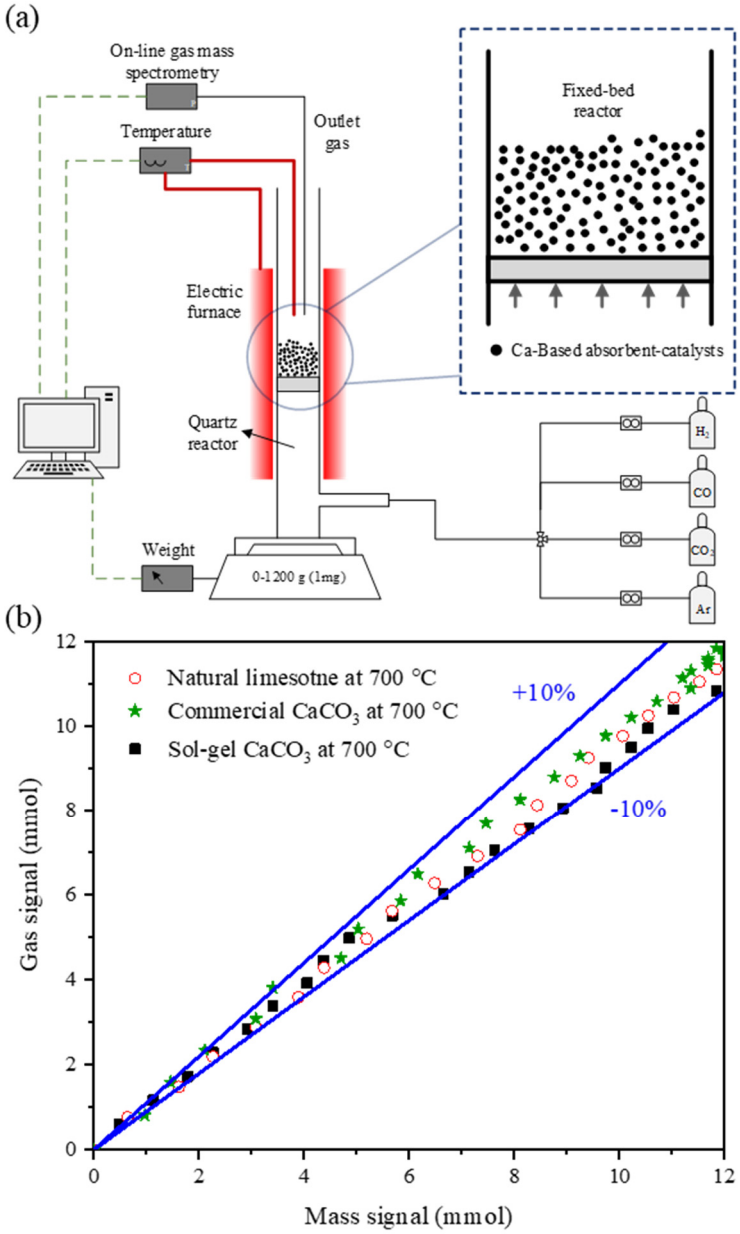

Figure 2. (**a**) Schematic diagram of the fixed−bed system coupled mass spectrometry system. (**b**) The consistency of gas signal and mass signal.

3. Results and Discussion

3.1. Phase and Structural Characterization of the Ca-Based DFMs

Figure 3a presents the XRD patterns of the fresh Ca-based dual functional materials (DFMs). The characteristic peaks of the $CaCO_3$ phase were detected in all the samples, and no impurity phases were observed, indicating the high purity of the three fresh DFMs. This purity is further confirmed by the detailed ICP results, as shown in Table S1. To further

investigate the surface properties, Raman spectra were obtained on fresh DFMs, as shown in Figure 3b. The Raman spectra of commercial $CaCO_3$ and sol-gel $CaCO_3$ reflected strong $CaCO_3$ peaks (151, 278, 709, 1083 cm^{-1}) and no carbon species on the sample surface. In contrast, the Raman spectra of natural limestone reflected carbon species, indicated by the D and G peaks at 1380 and 1586 cm^{-1}, respectively. Table 1 summarizes the carbon composition, main elements, surface area, and crystallite size. The carbon content on the natural limestone is consistent with carbon/sulfur analysis, indicating that the surface is slightly covered (0.03%) (Table S2). Figure 3c–e show SEM images and EDX mappings of Ca and O on the fresh DFMs. The EDX mappings reveal that the surface of all samples is evenly covered with elements Ca and O. This consistency aligns with the XRD and Raman results, where strong $CaCO_3$ diffraction peaks and Raman intensities were obtained, respectively. However, the SEM images indicate different morphologies among the three samples. Natural limestone and commercial $CaCO_3$ reveal smooth and dense surfaces, whereas sol-gel $CaCO_3$ shows a porous particle surface. This trend is similar to the BET results, with natural limestone and commercial $CaCO_3$ exhibiting relatively low surface areas (1.77 and 1.21 m^2 g^{-1}, respectively), while sol-gel $CaCO_3$ demonstrates a higher surface area (5.61 m^2 g^{-1}). The crystallite sizes of $CaCO_3$ were determined using the $CaCO_3$ (104) peak at 2 theta = 29.4° for all samples. The order of crystallite size increase was natural limestone (78.9 nm) > commercial $CaCO_3$ (58.9 nm) > sol-gel $CaCO_3$ (42.1 nm). The highest crystallite size of natural limestone may be attributed to the incorporation of trace metals, as indicated by the ICP results. Overall, the high purity of the DFMs, confirmed by these characterizations, makes them suitable candidates for the ICCU process.

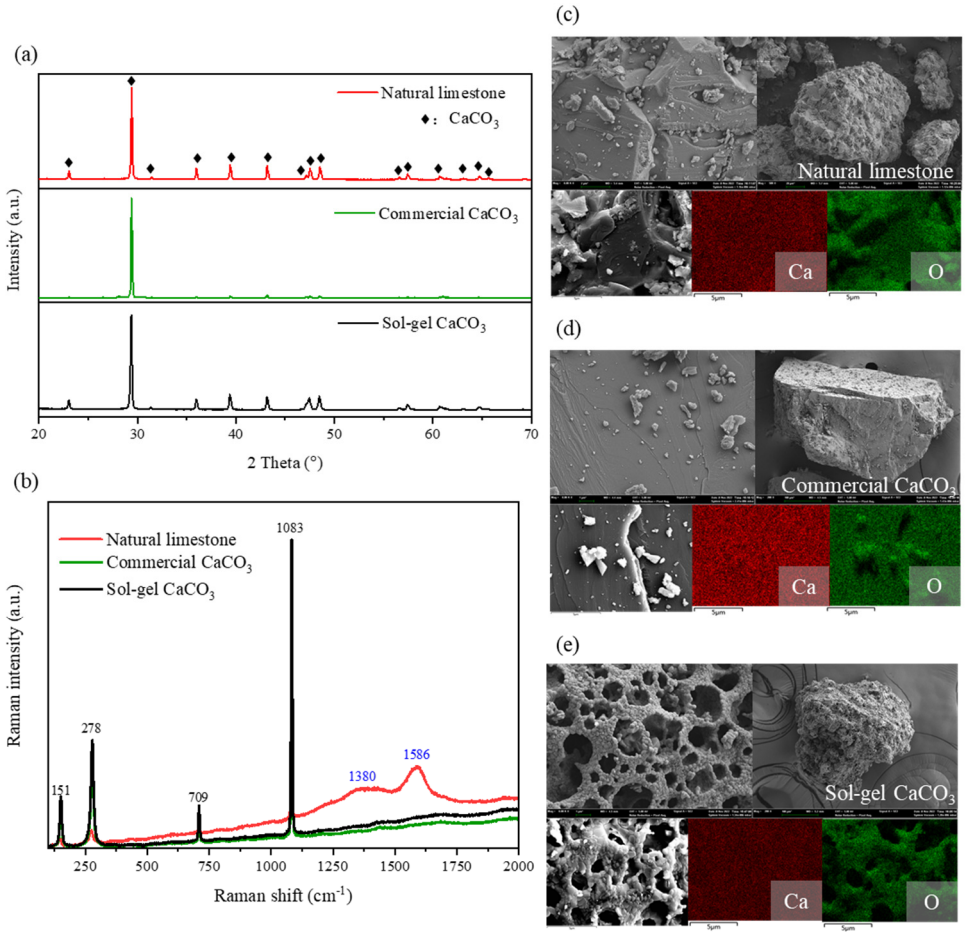

Figure 3. Characterization of the fresh Ca-based DFMs. (**a**) XRD pattern, (**b**) Raman spectra, SEM images and EDX mappings of (**c**) natural limestone, (**d**) commercial $CaCO_3$, and (**e**) sol−gel $CaCO_3$.

Table 1. Physical properties of the fresh Ca-based DFMs.

Sample	Carbon Composition (%)	Main Element (>0.01%)	BET Surface Area (m^2 g^{-1})	Crystallite Size (nm)
Natural limestone	0.03	Ca, Mg, Al, Fe, K, Sr	1.77	78.9
Commercial $DFMO_3$	-	Ca, Mg, Al	1.21	58.9
Sol-gel $DFMO_3$	-	Ca	5.61	42.1

3.2. Integrated CO_2 Capture and Utilization Performance of the Ca-Based DFMs

To determine the reaction region and pathway of carbonate hydrogenation, in situ FTIR and Temperature Programmed Surface Reaction (TPSR) analyses were conducted to elucidate the hydrogenation process on various DFMs (natural limestone, sol-gel $CaCO_3$, and commercial $CaCO_3$). The species were identified based on the absorbance intensities of their characteristic vibrational modes: ν(C=O) at 2337 cm^{-1} and 2360 cm^{-1} for CO_2, ν(C≡O) at 2171 cm^{-1} and 2113 cm^{-1} for CO, δ(H−O−H) at 1559 cm^{-1} for H_2O, and ν(C−H) at 3016 cm^{-1} for CH_4. Figure 4 illustrates a uniform single-step hydrogenation process across all samples, indicative of $CaCO_3$(s) → CaO(s) conversion. From the gas composition standpoint, the peak temperatures of CO_2 for sol-gel $CaCO_3$, commercial $CaCO_3$, and natural limestone were 706 °C, 726 °C, and 726 °C, respectively, indicating the unconverted CO_2 released from the sorbents of DFMs. Similarly, the peak temperatures of CO for sol-gel $CaCO_3$, commercial $CaCO_3$, and natural limestone were 706 °C, 736 °C, and 736 °C, respectively. The lowest peak temperature of CO for sol-gel $CaCO_3$ is likely due to its porous structure, which provides a better reaction interface during the hydrogenation process. Conversely, the presence of trace elements in natural limestone negatively impacted its reaction performance compared to sol-gel $CaCO_3$ and commercial $CaCO_3$. The inset in Figure 4 shows that in situ FTIR spectra analysis revealed the products were composed of CO_2 and CO, with no CH_4 detected. The absence of CH_4 suggests a high selectivity toward CO, especially at temperatures above 550 °C, primarily via the RWGS pathway. This observation aligns with the thermodynamic preference for CO production at higher temperatures and corroborates previous studies using CaO-alone material [30]. Therefore, the reaction temperature for this study was set between 650 °C and 750 °C.

Figure 5a illustrates the CO_2 capture and utilization performance using natural limestone in a fixed-bed system coupled with mass spectrometry at 700 °C. The reaction curves can be generally divided into three primary regions: CO_2 capture, inert gas purge, and hydrogenation processes. Initially, as $CaCO_3$ is the primary reactant, a portion of CO_2 is released during the heating stage, defining the first hydrogenation phase as the pre-hydrogenation stage. Following pre-hydrogenation, the system is purged with Ar to eliminate residual gases and subsequently exposed to simulated flue gas (15 vol% CO_2 balanced with Ar) for CO_2 capture. After Ar purging, a continuous flow of pure H_2 initiates the hydrogenation step within the fixed bed. The investigation focused on the three DFMs in terms of CO_2/CO/CH_4 yield, CO_2 conversion, and CO selectivity at 700 °C, as shown in Figure 5b. Notably, all DFMs demonstrated exceptional CO selectivity (~100%) with CO_2 conversions ranging between 75 and 81% without the addition of any catalyst components, leading to a lower cost compared to conventional DFMs. Among them, sol-gel $CaCO_3$ exhibited the highest CO yield (11.34 mmol g^{-1}), attributed to its higher CO_2 capture capacity (15.10 mmol g^{-1}) compared to natural limestone (13.96 mmol g^{-1}) and commercial $CaCO_3$ (12.49 mmol g^{-1}). This indicates that CO yield is strongly influenced by the CO_2 capture capacity of the DFMs. Figure 5c illustrates the impact of temperature on the reactivity of DFMs. Higher temperatures (e.g., 725 °C and 750 °C) resulted in lower CO_2 conversion (65–75%) across all DFMs. This suggests that the rapid decomposition rate of $CaCO_3$ at higher temperatures significantly influences the overall CO_2 conversion, leading to more unconverted CO_2 being released into the atmosphere. The increased reaction temperature correlated with an increased amount of unconverted CO_2 (blue bar), which presented a

similar trend across the performance of all three DFMs. Regarding CO selectivity, all DFMs demonstrated 100% selectivity during the hydrogenation process. Notably, sol-gel $CaCO_3$ maintained good reaction performance between 650 °C and 750 °C, indicating that the particle structure plays a key role during the reaction of CaO-alone material. Considering the reactive performance and efficiencies of DFMs in both CO_2 capture and utilization, the temperature of 700 °C was deemed optimal. Despite sol-gel $CaCO_3$ exhibiting the highest CO yield in CO_2 capture and conversion, the cost-effective and abundantly available natural limestone emerged as more competitive than synthesized and state-of-the-art dual functional materials.

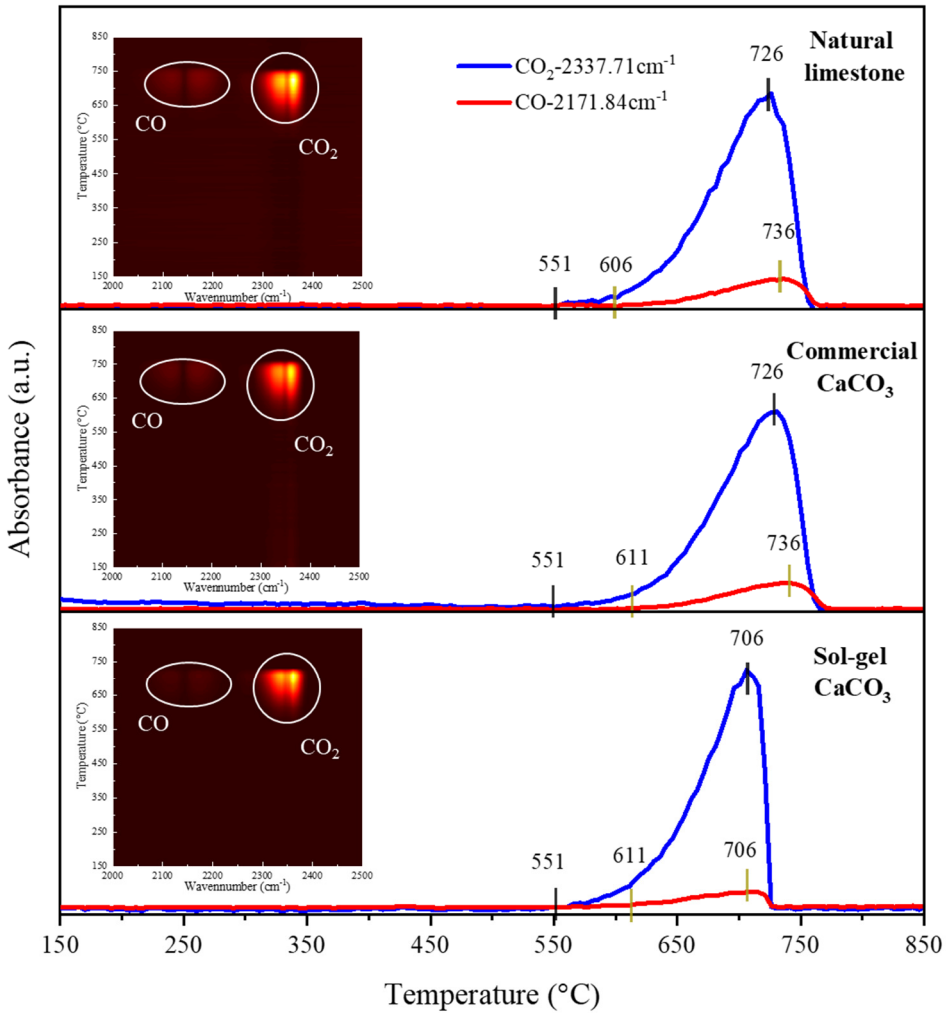

Figure 4. H_2−TPSR results of natural limestone, commercial $CaCO_3$, and sol−gel $CaCO_3$. The inlets depict in situ FTIR data in contour plots.

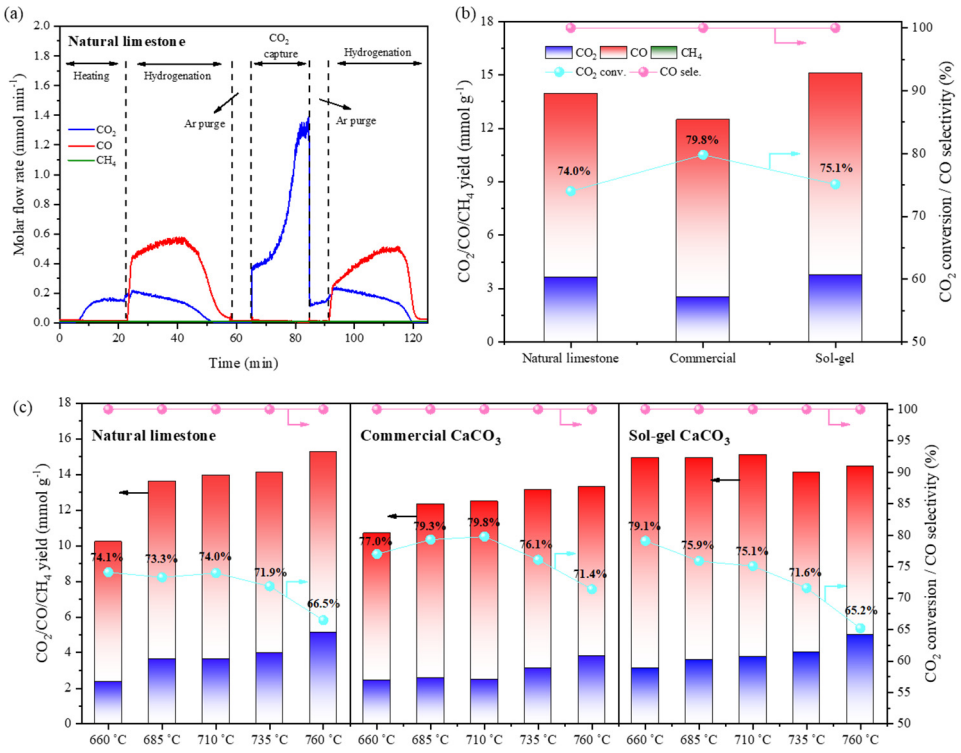

Figure 5. (**a**) One CO_2 capture and in situ hydrogenation cycle of natural limestone at 700 °C; (**b**) Ca−based DFMs on the CO_2/CO/CH_4 yield, CO_2 conversion, and CO selectivity at 700 °C; (**c**) the effect of temperature of Ca−based DFMs on the CO_2/CO/CH_4 yield, CO_2 conversion, and CO selectivity.

3.3. Cyclability of CO_2 Capture and Utilization on Ca-Based DFMs

To comprehensively understand the cyclability of the integrated CO_2 capture and utilization processes of the DFMs, a series of experiments were conducted using a fixed-bed system coupled with mass spectrometry at 700 °C over 20 cycles (Figure 6). The carbonation stage involved 15 vol% CO_2, and the hydrogenation stage involved pure H_2. Throughout the 20-cycle ICCU-RWGS process, all DFMs experienced a decline in CO_2 capture and carbonation conversion as the number of cycles increased. However, at the relatively mild reaction temperature of 700 °C (compared to the conventional calcination temperature of 850–900 °C in the calcium-looping process), the decrease in CO_2 capture capacity was slower, particularly for sol-gel $CaCO_3$. Specifically, in the initial cycle, natural limestone, commercial $CaCO_3$, and sol-gel $CaCO_3$ exhibited CO_2 capture capacities of 15.78 mmol g^{-1}, 16.23 mmol g^{-1}, and 15.10 mmol g^{-1}, respectively. By the 10th cycle, these capacities declined to 9.09 mmol g^{-1}, 8.76 mmol g^{-1}, and 10.88 mmol g^{-1}, respectively, corresponding to decreases of 42%, 46%, and 28%. By the 20th cycle, the capacities further reduced to 6.17 mmol g^{-1}, 6.65 mmol g^{-1}, and 8.44 mmol g^{-1}, representing decreases of 61%, 59%, and 44%, respectively. Notably, sol-gel $CaCO_3$ retained 58% of its CO_2 capture capacity after the 20-cycle carbonation and hydrogenation process, significantly higher than the 20–30% retention observed in conventional calcination processes [42]. Despite these declining trends in CO_2 capture capacity, the CO_2 conversion of the DFMs remained relatively stable, consistently in the 70–80% range. The average CO_2 conversion percentages for natural limestone, commercial $CaCO_3$, and sol-gel $CaCO_3$ were 71.76%, 76.05%, and 73.83%, respectively, indicating stability in the CO_2 conversion released from sorbents. Throughout the ICCU-RWGS process, all DFMs exhibited nearly 100% CO selectivity.

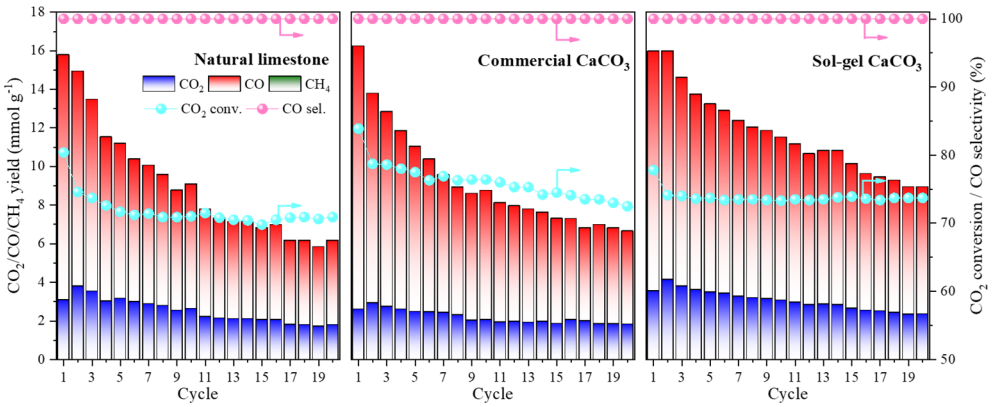

Figure 6. Twenty cycles of integrated CO_2 capture and utilization process on natural limestone, commercial $CaCO_3$, and sol−gel $CaCO_3$.

To date, there have been several studies on the ICCU-RWGS process using calcium-based DFMs. Table 2 presents a comparison of the ICCU-RWGS performance of Ca-based DFMs. The CO_2 capture capacity ranges from 8.95 to 16.2 mmol g^{-1} for fresh DFMs on both synthetic and natural materials, indicating high CO_2 capture performance in calcium-based materials. Regarding CO yield, most DFMs exhibit the capability of CO formation with high CO selectivity, including CaO-alone materials, with yields ranging from 6.9 to 13.6 mmol g^{-1} for fresh samples. This trend is also reflected in CO_2 conversion rates, which range from 46.0% to 96.4%. However, from a cyclic stability standpoint, natural and non-modified materials experience a rapid decline during cyclic reactions compared to synthetic materials. In terms of loss in capacity, marble dust exhibited a 30% decrease, followed by sol-gel $CaCO_3$ (44%), commercial $CaCO_3$ (59%), and natural limestone (61%). Synthetic materials demonstrated more stable cyclic performance during the ICCU-RWGS process. Notably, $Ca_1Ni_{0.1}Ce_{0.033}$ stands out as the best-performing DFM over 20 cycles, due to the well-dispersed CeO_2, which acts as a physical barrier that effectively prevents the growth and agglomeration of CaO crystallites and NiO species [39]. Therefore, given the outstanding performance in CO_2 capture capacity, CO_2 conversion, CO yield, and cyclic stability, appropriate modification of calcium-based materials for cyclic reactions is crucial.

Table 2. A comparison of ICCU-RWGS performance of Ca-based DFMs to those reported in literatures.

Sample	Conditions	CO_2 Capture Capacity (mmol g^{-1})	CO_2 Conversion (%)	CO Yield (mmol g^{-1})	Loss-in-Capacity (%)	Ref.
Mable dust	650 °C, 10% CO_2, 5% H_2	9.4	85.2	8.0	47 cycles, 30	[27]
$Fe_5Co_5Mg_{10}CaO$	650 °C, 10% CO_2, pure H_2	9.2	88.5	8.2	10 cycles, 4	[15]
CaO-$CaGa_{0.5}Zr_{0.5}$(O)	650 °C, 15% CO_2, pure H_2	14.55	87.8	12.29	20 cycles, 13	[33]
$Ca_1Ni_{0.1}$	650 °C, 15% CO_2, 5% H_2	15.0	46.0	6.9	20 cycles, 33	[39]
$Ca_1Ni_{0.1}Ce_{0.033}$		14.1	51.1	7.3	20 cycles, stable	
Ni/CS-P30-C	650 °C, 10% CO_2, 5% H_2	13.86	39.8	5.52	17 cycles, 49	[18]
stableNi/CS-P30-C-P		8.95	59.6	5.33	17 cycles, 26	
NiCaCe-SG	650 °C, 10% CO_2, 10% H_2	15.34	92.4	5.97	10 cycles, 12	[40]
Natural limestone	700 °C, 15% CO_2, pure H_2	15.8	81.1	12.7	20 cycles, 61	This study
Commercial $CaCO_3$		16.2	79.8	13.6	20 cycles, 59	
Sol-gel $CaCO_3$		15.1	75.1	11.7	20 cycles, 44	

To provide substantial evidence for elucidating the cyclic morphology of the spent DFM particles, SEM images in Figure 7 complement these findings by offering visual evidence of changes in the physical properties of the spent Ca-based DFMs after 20 cycles. After 20 cycles, some micro-grade pores were still present on the surface of sol-gel $CaCO_3$, although some areas showed signs of sintering. When zoomed in, cavities were visible inside the sol-gel $CaCO_3$. In contrast, natural limestone and commercial $CaCO_3$ appeared coarser and rougher, with few micro-grade pores remaining. According to Bhatia, a porous surface is beneficial for the carbonation reaction [43], indicating that sol-gel $CaCO_3$ absorbed CO_2 with high efficiency in the present study due to its abundant pores, which facilitate the diffusion of CO_2 into the surface of the DFM. This suggests better diffusion of CO_2 towards the CaO and more stable micro-structures of the sorbents, especially on sol-gel $CaCO_3$. This is in good agreement with the observation and previous study that the finer pores and skeleton structure of calcium-based material can mitigate agglomeration and sintering during the cyclic reactions [28,44]. Overall, a certain degree of sintering was observed in all DFMs. Among them, sol-gel $CaCO_3$ maintained a skeleton-like structure with micro-grade pores as the number of cycles increased, unlike the non-skeleton-like structure of natural limestone and commercial $CaCO_3$. This highlights the importance of modifying Ca-based materials to enhance their performance.

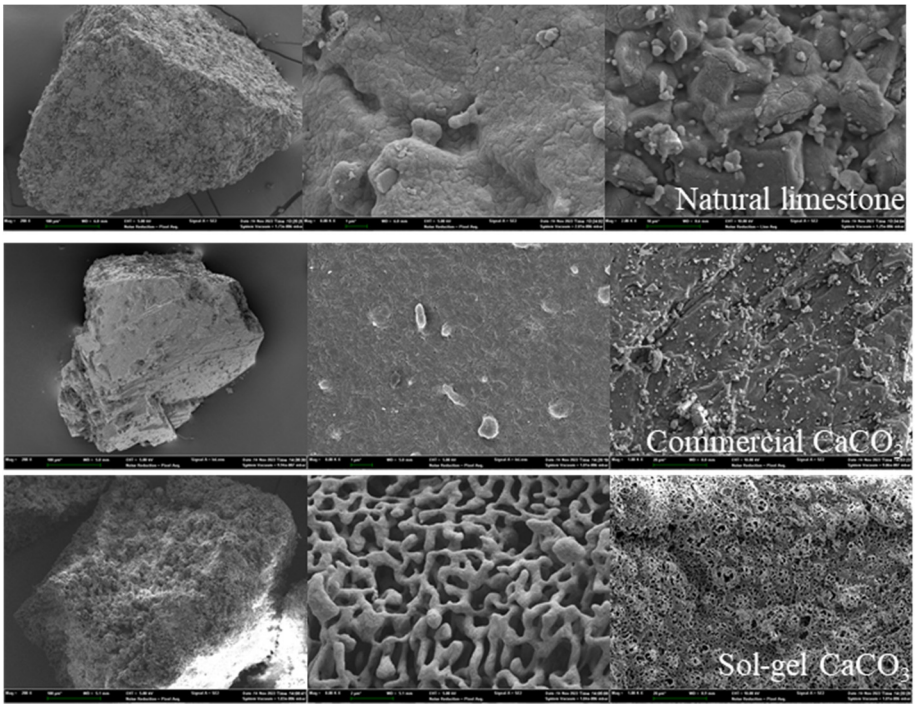

Figure 7. SEM images of natural limestone, commercial $CaCO_3$, and sol-gel $CaCO_3$ after 20 cycles at magnifications of 200×, 1000×, and 8000×.

4. Conclusions

This study investigated the CO_2 capture performance of CaO-alone dual functional materials (DFMs) prepared from natural limestone, commercially available carbonate, and synthetic materials (sol-gel $CaCO_3$). A comparative thermodynamic analysis of the three CaO-alone DFMs was performed over 20 cycles of the ICCU-RWGS process. Firstly, the in situ FTIR results revealed the dominance of the reverse water-gas shift reaction (RWGS) route instead of methanation and exhibited self-catalytic activity across all CaO-alone DFMs. Additionally, the influence of temperature on CO_2 conversion, CO yield, and cyclability was examined within the range of 650 to 750 °C. The results indicated that the loss in CO_2 capture capacity for the sol-gel $CaCO_3$ decreased from 15.1 to 8.44 mmol g^{-1} over 20 cycles. A certain level of deactivation occurred in the ICCU-RWGS process

due to CaO agglomeration. The abundant pores and skeleton structure inside the sol-gel $CaCO_3$ particles facilitated the diffusion of CO_2 into the surface of the sorbent, resulting in enhanced CO_2 capture performance compared to natural limestone and commercial $CaCO_3$. This study offers a promising pathway for CaO-alone DFMs to achieve carbon neutrality using ICCU technology.

Supplementary Materials: The following supporting information can be downloaded at: https://www.mdpi.com/article/10.3390/pr12081548/s1, Figure S1: One CO_2 capture and in situ hydrogenation cycle of commercial $CaCO_3$ at 700 °C; Figure S2: One CO_2 capture and in situ hydrogenation cycle of sol-gel $CaCO_3$ at 700 °C; Table S1: ICP results of natural limestone; Table S2: The carbon and sulfur content of natural limestone.

Author Contributions: Conceptualization, I.W. and Z.L.; validation, I.W. and S.W.; formal analysis, I.W.; writing—original draft preparation, I.W. and S.W.; writing—review and editing, I.W. and Z.L.; project administration, I.W. and Z.L.; funding acquisition, I.W. and Z.L. All authors have read and agreed to the published version of the manuscript.

Funding: This research was supported by the National Natural Science Foundation of China (Grant No. 52306150) and the financial support from China Postdoctoral Science Foundation (2023M741896).

Data Availability Statement: Data are contained within the article.

Acknowledgments: The authors wish to acknowledge the FLOTU (Fluidization Laboratory of Tsinghua University).

Conflicts of Interest: The authors declare no conflicts of interest.

References

1. Rogelj, J.; Den Elzen, M.; Höhne, N.; Fransen, T.; Fekete, H.; Winkler, H.; Schaeffer, R.; Sha, F.; Riahi, K.; Meinshausen, M. Paris Agreement climate proposals need a boost to keep warming well below 2 C. *Nature* **2016**, *534*, 631–639. [CrossRef] [PubMed]
2. Muslemani, H.; Liang, X.; Kaesehage, K.; Wilson, J. Business models for carbon capture, utilization and storage technologies in the steel sector: A qualitative multi-method study. *Processes* **2020**, *8*, 576. [CrossRef]
3. Lv, Z.; Du, H.; Xu, S.; Deng, T.; Ruan, J.; Qin, C. Techno-economic analysis on CO_2 mitigation by integrated carbon capture and methanation. *Appl. Energy* **2024**, *355*, 122242. [CrossRef]
4. Chen, J.; Xu, Y.; Liao, P.; Wang, H.; Zhou, H. Recent progress in integrated CO_2 capture and conversion process using dual function materials: A state-of-the-art review. *Carbon Capture Sci. Technol.* **2022**, *4*, 100052. [CrossRef]
5. Jin, B.; Wang, R.; Fu, D.; Ouyang, T.; Fan, Y.; Zhang, H.; Liang, Z. Chemical looping CO_2 capture and in-situ conversion as a promising platform for green and low-carbon industry transition: Review and perspective. *Carbon Capture Sci. Technol.* **2023**, *10*, 100169. [CrossRef]
6. Fernández, J.; Sotenko, M.; Derevschikov, V.; Lysikov, A.; Rebrov, E.V. A radiofrequency heated reactor system for post-combustion carbon capture. *Chem. Eng. Process. Process Intensif.* **2016**, *108*, 17–26. [CrossRef]
7. Ahmed, S.; Bibi, S.S.; Irshad, M.; Asif, M.; Khan, M.K.; Kim, J. Synthesis of long-chain paraffins over bimetallic Na–$Fe_{0.9}Mg_{0.1}O_x$ by direct CO_2 hydrogenation. *Top. Catal.* **2024**, *67*, 363–376. [CrossRef]
8. Ahmed, S.; Irshad, M.; Yoon, W.; Karanwal, N.; Sugiarto, J.R.; Khan, M.K.; Kim, S.K.; Kim, J. Evaluation of MgO as a promoter for the hydrogenation of CO_2 to long-chain hydrocarbons over Fe-based catalysts. *Appl. Catal. B Environ.* **2023**, *338*, 123052. [CrossRef]
9. Qiao, Y.; Liu, W.; Guo, R.; Sun, S.; Zhang, S.; Bailey, J.J.; Fang, M.; Wu, C. Techno-economic analysis of integrated carbon capture and utilisation compared with carbon capture and utilisation with syngas production. *Fuel* **2023**, *332*, 125972. [CrossRef]
10. Lv, Z.; Deng, T.; Gao, C.; Zheng, Y.; Wu, C.; Ran, J.; Qin, C. Promotion of active H-assisted $CaCO_3$ conversion for integrated CO_2 capture and methanation. *Chem. Eng. J.* **2024**, *489*, 151427. [CrossRef]
11. Boukha, Z.; Bermejo-López, A.; De-La-Torre, U.; González-Velasco, J.R. Behavior of nickel supported on calcium-enriched hydroxyapatite samples for CCU-methanation and ICCU-methanation processes. *Appl. Catal. B Environ.* **2023**, *338*, 122989. [CrossRef]
12. Sun, S.; Wang, Y.; Xu, Y.; Sun, H.; Zhao, X.; Zhang, Y.; Yang, X.; Bie, X.; Wu, M.; Zhang, C. Ni-functionalized Ca@Si yolk-shell nanoreactors for enhanced integrated CO_2 capture and dry reforming of methane via confined catalysis. *Appl. Catal. B Environ. Energy* **2024**, *348*, 123838. [CrossRef]
13. Li, J.; Gao, C.; Cheng, Y.; Lv, Z.; Qin, C. Solar driven integrated CO_2 capture and CH_4 dry reforming via Fe_xMn_y/Ni/CaAl multi-function materials. *Chem. Eng. J.* **2024**, *490*, 151512. [CrossRef]
14. Sun, S.; Zhang, C.; Guan, S.; Xu, S.; Williams, P.T.; Wu, C. Ni/support-CaO bifunctional combined materials for integrated CO_2 capture and reverse water-gas shift reaction: Influence of different supports. *Sep. Purif. Technol.* **2022**, *298*, 121604. [CrossRef]

15. Shao, B.; Hu, G.; Alkebsi, K.A.; Ye, G.; Lin, X.; Du, W.; Hu, J.; Wang, M.; Liu, H.; Qian, F. Heterojunction-redox catalysts of $Fe_xCo_yMg_{10}CaO$ for high-temperature CO_2 capture and in situ conversion in the context of green manufacturing. *Energy Environ. Sci.* **2021**, *14*, 2291–2301. [CrossRef]
16. Wang, I.; Cai, J.; Wang, S.; Li, Z. Uncovering hydrogen-to-carbon ratio for integrated CO_2 capture and reverse water-gas shift reaction through MFB-TGA-MS analysis. *Sep. Purif. Technol.* **2025**, *353*, 128601. [CrossRef]
17. Xie, Z.; Sun, Z.; Shao, B.; Zhu, Y.; Ma, R.; Li, S.; Li, J.; Chen, Y.; Liu, H.; Hu, J. Highly efficient hydrogenation of carbonate to methanol for boosting CO_2 mitigation. *Chem. Eng. J.* **2024**, *495*, 153465. [CrossRef]
18. Wang, G.; Guo, Y.; Yu, J.; Liu, F.; Sun, J.; Wang, X.; Wang, T.; Zhao, C. Ni-CaO dual function materials prepared by different synthetic modes for integrated CO_2 capture and conversion. *Chem. Eng. J.* **2022**, *428*, 132110. [CrossRef]
19. Zhang, Y.; Zhao, S.; Li, L.; Feng, J.; Li, K.; Huang, Z.; Lin, H. Integrated CO_2 capture and utilization: A review of the synergistic effects of dual function materials. *Catal. Sci. Technol.* **2024**, *14*, 790–819. [CrossRef]
20. Huang, P.; Chu, J.; Fu, J.; Yu, J.; Li, S.; Guo, Y.; Zhao, C.; Liu, J. Influence of reduction conditions on the structure-activity relationships of $NaNO_3$-promoted Ni/MgO dual function materials for integrated CO_2 capture and methanation. *Chem. Eng. J.* **2023**, *467*, 143431. [CrossRef]
21. Li, J.; He, X.; Hu, R. Integrated Carbon Dioxide Capture and Utilization for the Production of CH_4, Syngas and Olefins over Dual-Function Materials. *ChemCatChem* **2024**, e202301714. [CrossRef]
22. Bermejo-López, A.; Pereda-Ayo, B.; Onrubia-Calvo, J.A.; González-Marcos, J.A.; González-Velasco, J.R. How the presence of O_2 and NOx influences the alternate cycles of CO_2 adsorption and hydrogenation to CH_4 on Ru-Na-Ca/Al_2O_3 dual function material. *J. CO2 Util.* **2023**, *67*, 102343. [CrossRef]
23. Proaño, L.; Tello, E.; Arellano-Trevino, M.A.; Wang, S.; Farrauto, R.J.; Cobo, M. In-situ DRIFTS study of two-step CO_2 capture and catalytic methanation over Ru, "Na_2O"/Al_2O_3 Dual Functional Material. *Appl. Surf. Sci.* **2019**, *479*, 25–30. [CrossRef]
24. Lv, Z.; Chen, S.; Huang, X.; Qin, C. Recent progress and perspective on integrated CO_2 capture and utilization. *Curr. Opin. Green Sustain. Chem.* **2023**, *40*, 100771. [CrossRef]
25. Liu, G.; Hu, Z.; Lisak, G. CO_2 capture and utilization through isothermal carbonation-calcination looping integrated with MSW pyrolysis volatile reforming. *Chem. Eng. J.* **2024**, *482*, 149164. [CrossRef]
26. Jo, S.; Lee, J.H.; Woo, J.H.; Kim, T.-Y.; Ryu, H.-J.; Hwang, B.; Kim, J.C.; Lee, S.C.; Gilliard-AbdulAziz, K.L. Coke-promoted Ni/CaO catal-sorbents in the production of cyclic CO and syngas. *Sustain. Energy Fuels.* **2022**, *6*, 81–88. [CrossRef]
27. Sun, S.; Wang, Y.; Zhao, X.; Zhang, C.; Wu, C. One step upcycling CO_2 from flue gas into CO using natural stone in an integrated CO_2 capture and utilisation system. *Carbon Capture Sci. Technol.* **2022**, *5*, 100078. [CrossRef]
28. Li, Z.-S.; Cai, N.-S.; Huang, Y.-Y.; Han, H.-J. Synthesis, experimental studies, and analysis of a new calcium-based carbon dioxide absorbent. *Energy Fuels* **2005**, *19*, 1447–1452. [CrossRef]
29. Sun, S.; Lv, Z.; Qiao, Y.; Qin, C.; Xu, S.; Wu, C. Integrated CO_2 capture and utilization with CaO-alone for high purity syngas production. *Carbon Capture Sci. Technol.* **2021**, *1*, 100001. [CrossRef]
30. Wang, I.; Li, D.; Wang, S.; Wang, Y.; Lin, G.; Yan, B.; Li, Z. Limestone hydrogenation combined with reverse water–gas shift reaction under fluidized and iso-thermal conditions using MFB-TGA-MS. *Chem. Eng. J.* **2023**, *472*, 144822. [CrossRef]
31. Sun, H.; Wang, Y.; Xu, S.; Osman, A.I.; Stenning, G.; Han, J.; Sun, S.; Rooney, D.; Williams, P.T.; Wang, F. Understanding the interaction between active sites and sorbents during the integrated carbon capture and utilization process. *Fuel* **2021**, *286*, 119308. [CrossRef]
32. Han, R.; Wang, Y.; Wei, L.; Peng, M.; Li, Z.; Liu, C.; Liu, Q. Integrated CO_2 capture and conversion by Cu/CaO dual function materials: Effect of in-situ conversion on the sintering of CaO and its CO_2 capture performance. *Carbon Capture Sci. Technol.* **2024**, *12*, 100220. [CrossRef]
33. Zhou, Y.; Ma, X.; Yusanjan, Q.; Cui, H.; Cheng, Z.; Zhou, Z. Active metal-free CaO-based dual-function materials for integrated CO_2 capture and reverse water–gas shift. *Chem. Eng. J.* **2024**, *485*, 149937. [CrossRef]
34. Sun, H.; Zhang, Y.; Guan, S.; Huang, J.; Wu, C. Direct and highly selective conversion of captured CO_2 into methane through integrated carbon capture and utilization over dual functional materials. *J. CO2 Util.* **2020**, *38*, 262–272. [CrossRef]
35. Sun, S.; Chen, Z.; Xu, Y.; Wang, Y.; Zhang, Y.; Dejoie, C.; Xu, S.; Xu, X.; Wu, C. Potassium-Promoted Limestone for Preferential Direct Hydrogenation of Carbonates in Integrated CO_2 Capture and Utilization. *JACS Au* **2023**, *4*, 72–79. [CrossRef] [PubMed]
36. Jo, S.; Lee, J.H.; Kim, T.Y.; Woo, J.H.; Ryu, H.-J.; Hwang, B.; Lee, S.C.; Kim, J.C.; Gilliard-AbdulAziz, K.L. A fundamental study of CO_2 capture and CH_4 production in a rapid cyclic system using nickel-lithium-silicate as a catal-sorbent. *Fuel* **2022**, *311*, 122602. [CrossRef]
37. Woo, J.-H.; Jo, S.; Kim, J.-E.; Kim, T.-Y.; Son, H.-D.; Ryu, H.-J.; Hwang, B.; Kim, J.-C.; Lee, S.-C.; Gilliard-AbdulAziz, K.L. Effect of the Ni-to-CaO Ratio on Integrated CO_2 Capture and Direct Methanation. *Catalysts* **2023**, *13*, 1174. [CrossRef]
38. Wang, S.; Cai, J.; Wang, I.; Li, Z. An experimental and kinetic modeling study of CO_2 hydrogenation to CO over Cu-Al catalyst utilizing MFB-TGA-MS. *Carbon Capture Sci. Technol.* **2024**, *10*, 100163. [CrossRef]
39. Sun, H.; Wang, J.; Zhao, J.; Shen, B.; Shi, J.; Huang, J.; Wu, C. Dual functional catalytic materials of Ni over Ce-modified CaO sorbents for integrated CO_2 capture and conversion. *Appl. Catal. B Environ.* **2019**, *244*, 63–75. [CrossRef]
40. Wu, J.; Zheng, Y.; Fu, J.; Guo, Y.; Yu, J.; Chu, J.; Huang, P.; Zhao, C. Synthetic Ni–CaO–CeO_2 dual function materials for integrated CO_2 capture and conversion via reverse water–gas shift reaction. *Sep. Purif. Technol.* **2023**, *317*, 123916. [CrossRef]

41. Wang, I.; Huang, S.; Wang, S.; Bie, X.; Zhou, H.; Li, Z. Mechanistic study of integrated CO_2 capture and utilization over Cu and Al-modified calcined limestone with high stability using MFB-TGA-MS. *Sep. Purif. Technol.* **2024**, *333*, 125975. [CrossRef]
42. Xu, Y.; Luo, C.; Zheng, Y.; Ding, H.; Zhou, D.; Zhang, L. Natural Calcium-Based Sorbents Doped with Sea Salt for Cyclic CO_2 Capture. *Chem. Eng. Technol.* **2017**, *40*, 522–528. [CrossRef]
43. Bhatia, S.; Perlmutter, D. Effect of the product layer on the kinetics of the CO_2-lime reaction. *AIChE J.* **1983**, *29*, 79–86. [CrossRef]
44. Wang, S.; Wang, I.; Li, Z. Metal oxide and nitrate-modified calcium gluconate-based sorbent with high stability for integrated carbon capture and utilization process. *Sep. Purif. Technol.* **2024**, *330*, 125502. [CrossRef]